



# Photocatalytic and antibacterial properties of Au-decorated $\text{Fe}_3\text{O}_4/\text{mTiO}_2$ core-shell microspheres

Cuiyan Li<sup>a,c</sup>, Reza Younesi<sup>a</sup>, Yanling Cai<sup>b</sup>, Yihua Zhu<sup>c</sup>, Mingguo Ma<sup>d</sup>, Jiefang Zhu<sup>a,\*</sup>

<sup>a</sup> Department of Chemistry - Ångström Laboratory, Uppsala University, Uppsala 75121, Sweden

<sup>b</sup> Division of Nanotechnology and Functional Materials, Ångström Laboratory, Uppsala University, Uppsala 75121, Sweden

<sup>c</sup> Key Laboratory for Ultrafine Materials of Ministry of Education, East China University of Science and Technology, Shanghai 200237, China

<sup>d</sup> Institute of Biomass Chemistry and Technology, College of Materials Science and Technology, Beijing Forestry University, Beijing 100083, China

## ARTICLE INFO

### Article history:

Received 17 January 2014

Received in revised form 4 March 2014

Accepted 11 March 2014

Available online 24 March 2014

### Keywords:

$\text{Fe}_3\text{O}_4$  microsphere  
Mesoporous  $\text{TiO}_2$   
Core-shell structure  
Au nanoparticle  
Photocatalysis  
Antibacterial effect  
Recycle

## ABSTRACT

A facile approach for the fabrication of Au-decorated mesoporous  $\text{Fe}_3\text{O}_4/\text{TiO}_2$  ( $\text{Fe}_3\text{O}_4/\text{mTiO}_2$ ) core-shell microspheres is demonstrated. The protocol involved the coating of a successive layer of  $\text{TiO}_2$  onto a magnetic  $\text{Fe}_3\text{O}_4$  core via a sol-gel process, followed by  $\text{TiO}_2$  crystallization and mesopore-formation by a hydrothermal treatment, and then the deposition of Au nanoparticles onto  $\text{Fe}_3\text{O}_4/\text{mTiO}_2$  microspheres through an *in situ* reduction of perchloric acid. The mesoporous microspheres ( $\text{Fe}_3\text{O}_4/\text{mTiO}_2$ ) showed stronger magnetic properties than the dense sample ( $\text{Fe}_3\text{O}_4/\text{TiO}_2$ ) before the hydrothermal treatment. The size and loading amount of Au nanoparticles were controlled by the reduction temperature and concentration of Au salt, respectively. Compared to unmodified  $\text{Fe}_3\text{O}_4/\text{mTiO}_2$  microspheres,  $\text{Fe}_3\text{O}_4/\text{mTiO}_2/\text{Au}$  microspheres showed higher photocatalytic activity for organic degradation and antibacterial action in water. These core-shell  $\text{Fe}_3\text{O}_4/\text{mTiO}_2/\text{Au}$  microspheres can serve as efficient and recyclable photocatalysts, which have promising applications in environmental treatment.

© 2014 Elsevier B.V. All rights reserved.

## 1. Introduction

During the past decades, photocatalytic degradation of organic pollutants in water by using semiconductor nanoparticles has attracted intense attention. Among various photocatalysts, titania ( $\text{TiO}_2$ ) has been proven the most suitable for widespread environmental applications due to its high chemical stability, non-toxicity, and excellent degradation capacity [1,2]. However, on the basis of practicality, although monodispersed  $\text{TiO}_2$  nanomaterials with high surface area and excellent photocatalytic activity have been successfully prepared [3–5], one of the major disadvantages for the application of such nanomaterials in water treatment is the inconvenience to recycle these photocatalysts due to their good dispersive properties. Conventional separation methods, including centrifugation and filtration, may lead to catalyst loss and energy consumption. Even though photocatalysts fixed on thin films allowing easy recovery have been successfully prepared [6–11], the activity of such photocatalysts is considerably reduced, because the effective surface area is significantly decreased.

In recent years, immobilizing catalysts onto magnetic nano- or microparticles has been adopted to solve the problem described above, as the catalysts can be easily collected from the solution with the help of an external magnetic field. There are two methods for immobilizing catalysts (e.g.  $\text{TiO}_2$ ) onto magnetic nano- or microparticles (e.g.  $\text{Fe}_3\text{O}_4$ ): indirect way and direct way. The indirect method has been developed to modify  $\text{Fe}_3\text{O}_4/\text{TiO}_2$  microstructure with an intermediate layer (e.g.  $\text{SiO}_2$ ), which is used as a barrier to avoid interactions between the magnetic core and the  $\text{TiO}_2$  coating during calcination [12], while the superparamagnetic characteristic of the hybrid nanoparticles significantly decreased. In order to avoid this disadvantage, a direct way has also been adopted to directly deposit  $\text{TiO}_2$  onto the magnetic cores. Xuan et al. have reported the fabrication of magnetically-separable photocatalysts with hollow nanostructures through a poly(styrene-acrylic acid) (PSA) template method at relatively low temperature [13], whereas, this method for preparing magnetic photocatalysts was relatively complicated. Therefore, the synthesis of magnetic photocatalysts has become a pressing need not only for fundamental interest but also for practical application.

It is well known that the wide band gap and low quantum yield of  $\text{TiO}_2$  limit its practical applications [14]. Improvement of the photocatalytic activity of  $\text{TiO}_2$  is an important task in heterogeneous photocatalysis. Noble metals, such as Au, Ag, Pt and Pd deposited

\* Corresponding author. Tel.: +46 18 4713722; fax: +46 18 153548.

E-mail addresses: [jiefang.zhu@kemi.uu.se](mailto:jiefang.zhu@kemi.uu.se), [jiefangzhu@hotmail.com](mailto:jiefangzhu@hotmail.com) (J. Zhu).

on  $\text{TiO}_2$  can achieve this goal, which is mainly due to the noble metals promoting the interfacial charge transfer processes in the composites [9,15–19]. Au-loaded  $\text{TiO}_2$  photoreaction systems can work for long hours, since Au deposits are relatively stable. Several representative methods have been reported on the introduction of Au nanoparticles on  $\text{TiO}_2$  such as electrodeposition [20], UV photoreduction [21], and chemical reduction [18]. However, most of the conventional methods failed to offer uniform distribution of Au nanoparticles on  $\text{TiO}_2$ , and the incorporated Au nanoparticles were usually loosely attached to  $\text{TiO}_2$ .

Although immobilizing  $\text{TiO}_2$  onto  $\text{Fe}_3\text{O}_4$  has been reported, as well as the deposition of Au nanoparticles on surface of  $\text{TiO}_2$  powder or film, few works have been carried out to combine  $\text{Fe}_3\text{O}_4$ ,  $\text{TiO}_2$  and Au to obtain a multifunctional photocatalyst [22,23]. The aim of this work is to prepare magnetically separable, recyclable, efficient photocatalysts through a simple method. The  $\text{Fe}_3\text{O}_4@ \text{TiO}_2$  microspheres with a core-shell structure were fabricated by a direct deposition of titania via a *sol-gel* process. The mesoporous  $\text{TiO}_2$  ( $\text{mTiO}_2$ ) shell was obtained by hydrothermally treating the as-synthesized  $\text{Fe}_3\text{O}_4@ \text{TiO}_2$  microspheres in a mixed ethanol/water solvent, using  $\text{NH}_3 \cdot \text{H}_2\text{O}$  as a porosity modifier. The anatase  $\text{TiO}_2$  nanoparticles on  $\text{Fe}_3\text{O}_4$  microspheres exhibited considerable photocatalytic activity, due to their large surface area and high crystallinity. Au nanoparticles, which were well dispersed on the  $\text{Fe}_3\text{O}_4@ \text{TiO}_2$  microspheres by *in situ* reduction of  $\text{Au}^{3+}$ , combined with  $\text{TiO}_2$  to form Au- $\text{TiO}_2$  heterostructure that can improve the separation of photogenerated electron-hole pairs, and thus enhance the photocatalytic activity of the  $\text{Fe}_3\text{O}_4@ \text{mTiO}_2$  microspheres. These  $\text{Fe}_3\text{O}_4@ \text{mTiO}_2@ \text{Au}$  microspheres possess unique multicomponent structures and multifunctional features, which could also have their potentials in other catalytic applications (e.g. CO oxidation) [24].

## 2. Experiment

### 2.1. Chemicals and materials

All chemicals, including  $\text{FeCl}_3 \cdot 6\text{H}_2\text{O}$ ,  $\text{NH}_4\text{Ac}$ , sodium citrate, ethylene glycol, ethanol, acetonitrile,  $\text{NH}_3 \cdot \text{H}_2\text{O}$ , tetrabutylorthotitanate (TBOT),  $\text{HAuCl}_4 \cdot 4\text{H}_2\text{O}$ , lysine,  $\text{NaBH}_4$  and methylene blue (MB), were analytical grade reagents, purchased from Sigma-Aldrich, and used without further purification.

### 2.2. Methods

#### 2.2.1. Preparation of $\text{Fe}_3\text{O}_4$ microspheres

The magnetite colloidal nanocrystal clusters were prepared through a modified solvothermal reaction [25,26]. Typically, 1.350 g of  $\text{FeCl}_3 \cdot 6\text{H}_2\text{O}$ , 3.854 g of  $\text{NH}_4\text{Ac}$ , and 0.400 g of sodium citrate were dissolved in 70 mL of ethylene glycol. The mixture was stirred vigorously for 1 h at  $170^\circ\text{C}$  to form a homogeneous black solution, and then transferred into a Teflon-lined stainless-steel autoclave (100 mL capacity). The autoclave was heated to  $200^\circ\text{C}$ , and maintained for 16 h; then it was cooled to room temperature. The black product was washed with ethanol and collected with the help of a magnet. The cycle of washing and magnetic separation was repeated several times.

To investigate the stability of the  $\text{Fe}_3\text{O}_4$  microspheres in polar solvents, which is important for evenly coating  $\text{TiO}_2$  onto them in the next step, 5 mg of the as-prepared  $\text{Fe}_3\text{O}_4$  microspheres was dispersed in 20 mL of deionized water and ethanol after ultra-sonic treatment, respectively. After 24 h, a majority of the black  $\text{Fe}_3\text{O}_4$  microspheres were still suspended, indicating that these  $\text{Fe}_3\text{O}_4$  microspheres have a good stability in water and ethanol, due to the stabilization by citrate on the microsphere surface.

#### 2.2.2. Coating $\text{Fe}_3\text{O}_4$ microspheres by $\text{TiO}_2$ to obtain $\text{Fe}_3\text{O}_4@ \text{TiO}_2$

The  $\text{Fe}_3\text{O}_4@ \text{TiO}_2$  core-shell microspheres were synthesized by directly coating a  $\text{TiO}_2$  layer on the  $\text{Fe}_3\text{O}_4$  in a mixed solvent of ethanol and acetonitrile by hydrolyzing TBOT in the presence of ammonia [27]. Briefly, 50 mg of the as-prepared  $\text{Fe}_3\text{O}_4$  was dispersed in a mixed solvent containing 90 mL of ethanol and 30 mL of acetonitrile with the aid of ultrasound, and then 0.5 mL of  $\text{NH}_3 \cdot \text{H}_2\text{O}$  was added. Finally, 1 mL of TBOT was added to the above suspension under stirring. After 1.5 h reaction, the products were collected by magnetic separation and washed several times with ethanol and acetonitrile.

#### 2.2.3. Hydrothermal treatment of $\text{Fe}_3\text{O}_4@ \text{TiO}_2$ to obtain $\text{Fe}_3\text{O}_4@ \text{mTiO}_2$

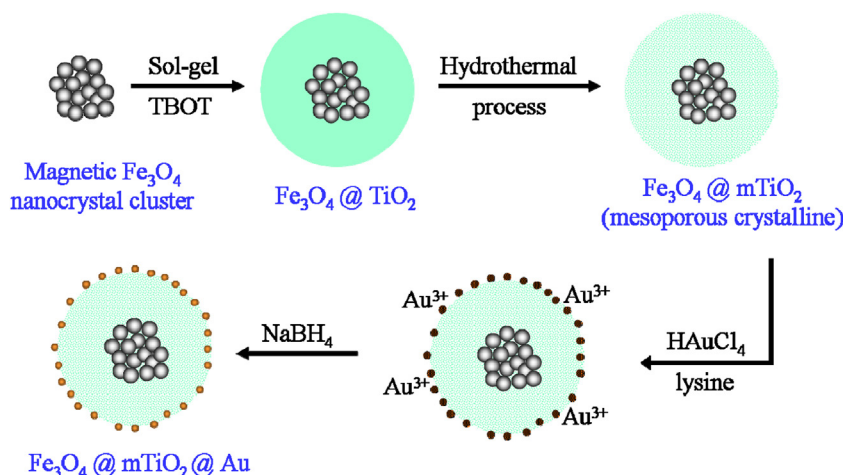
The mesoporous  $\text{TiO}_2$  shells were achieved by a hydrothermal treatment of the obtained  $\text{Fe}_3\text{O}_4@ \text{TiO}_2$  microspheres in a mixed solvent of ethanol and deionized water, with  $\text{NH}_3 \cdot \text{H}_2\text{O}$  as a porosity modifier. Typically, 50 mg of the as-synthesized  $\text{Fe}_3\text{O}_4@ \text{TiO}_2$  microspheres was dispersed in 40 mL of ethanol and 20 mL of deionized water, and then a certain amount of  $\text{NH}_3 \cdot \text{H}_2\text{O}$  (1 mL, 2 mL, or 3 mL) was added to the above suspension. The mixture was then transferred to a Teflon-lined stainless-steel autoclave (100 mL capacity), which was heated to  $160^\circ\text{C}$  and maintained for 20 h. Then the autoclave was cooled to room temperature, and the black product was collected with the help of a magnet, and washed with ethanol and water.

#### 2.2.4. Loading Au nanoparticles to obtain $\text{Fe}_3\text{O}_4@ \text{mTiO}_2@ \text{Au}$

The deposition of Au nanoparticles onto  $\text{Fe}_3\text{O}_4@ \text{mTiO}_2$  was performed as follows. 20 mg of  $\text{Fe}_3\text{O}_4@ \text{mTiO}_2$  core-shell microspheres was dispersed into 5 mL deionized water by ultrasonication for 15 min, and followed by the addition of a certain amount (V) of 0.01 M  $\text{HAuCl}_4$  (V is 1 mL, 2 mL, 3 mL, 4 mL, or 5 mL; the corresponding samples are denoted as  $\text{Fe}_3\text{O}_4@ \text{mTiO}_2@ \text{Au}_X$  mL or FTAX for short, where X presents the volume of  $\text{HAuCl}_4$  solution used in preparation) and the double amount (2 V) of 0.01 M lysine solution. The dispersion was stirred for 30 min. 2 V amount of 0.1 M fresh  $\text{NaBH}_4$  (excess) solution was added to reduce  $\text{HAuCl}_4$  to Au nanoparticles, and then deionized water was added to make the total volume up to 30 mL. After the solution being stirred at a certain temperature ( $60^\circ\text{C}$ ,  $70^\circ\text{C}$ ,  $80^\circ\text{C}$ , or  $90^\circ\text{C}$ ) for 1 h, the precipitate was collected by magnetic separation, washed several times with deionized water and ethanol, dried at  $70^\circ\text{C}$ , and calcined at  $300^\circ\text{C}$  in air for 1 h to remove lysine.

### 2.3. Characterization

The crystal structure of samples was analyzed by an X-ray diffractometer (Bruker, D8 Advance Twin/Twin) with  $\text{Cu K}\alpha$  radiation ( $\lambda = 1.54 \text{ \AA}$ ) at 45 kV and 40 mA. Transmission electron microscopy (TEM) micrographs were taken with a Tecnai F30 transmission electron microscope (FEI Company) using an accelerating voltage of 300 kV, which was equipped with an energy dispersive X-ray spectrometer (EDX) operated at 40 kV. For TEM observations, the sample powders were dispersed in ethanol by ultrasonic irradiation, and a drop of the suspension was placed onto a carbon-coated copper grid (Ted Pella, US). The deposit was dried in air prior to observation. In order to prove the core-shell structure of  $\text{Fe}_3\text{O}_4@ \text{TiO}_2$  composite, sample was analyzed by elemental mapping image analysis using electron energy loss spectroscopy (EELS). The XPS measurements were performed on a commercial PHI 5500 spectrometer, using monochromatic  $\text{Al K}\alpha$  radiation (1487 eV) and an electron emission angle of  $45^\circ$ . To reduce the effect of differential charging on samples, a flood gun was used during the measurements. All spectra were calibrated using the hydrocarbon peak



**Scheme 1.** Illustration of synthetic procedure for the mesoporous  $\text{Fe}_3\text{O}_4@m\text{TiO}_2@Au$  core-shell microspheres.

positioned at binding energy 285.0 eV.  $N_2$  adsorption–desorption experiments were performed on a Micromeritics ASAP 2020. The samples were degassed, dried over night at  $150^\circ\text{C}$ , and then analyzed at 77 K. Thermogravimetric and differential thermal analyses (TG-DTA) were carried out with a STA-409PC/4/H Luxx simultaneous TG-DTA/DSC apparatus (Netzsch, Germany) at a heating rate of  $5^\circ\text{C min}^{-1}$  under high-purity  $N_2$  flow at  $40\text{ mL min}^{-1}$ .

#### 2.4. Photocatalytic activity

Methylene blue (MB) was chosen as a model pollutant to evaluate photocatalytic activity of the as-prepared catalysts. In photocatalytic experiments, powder samples (15 mg) were added to an aqueous MB solution (60 mL, 8 mg/L), and the reaction

mixture was stirred in the dark for 30 min to ensure the adsorption/desorption equilibrium of the dye on the microspheres. Subsequently, the solution was exposed to UV radiation from four 9 W black lights (Philips) with the main emission wavelength at 365 nm. The illumination intensity at the sample level ( $160\text{ W/m}^2$ ) was measured with a pyranometer (Kipp & Zonen CM11), and the total flux can be estimated to be 1.6 W. 1 mL of MB solution was taken out, the photocatalyst powders were removed by a filter, and then the solution was analyzed with a UV–Vis spectrophotometer (HR2000, Ocean Optics). The progress in photodegradation of MB was estimated using the following equation:  $C/C_0 = I/I_0$ , where  $C_0$  and  $C$  represent the initial and real-time concentrations of MB, and  $I_0$  and  $I$  are the initial and real-time absorbances of MB at the characteristic absorption wavelength of 665 nm.

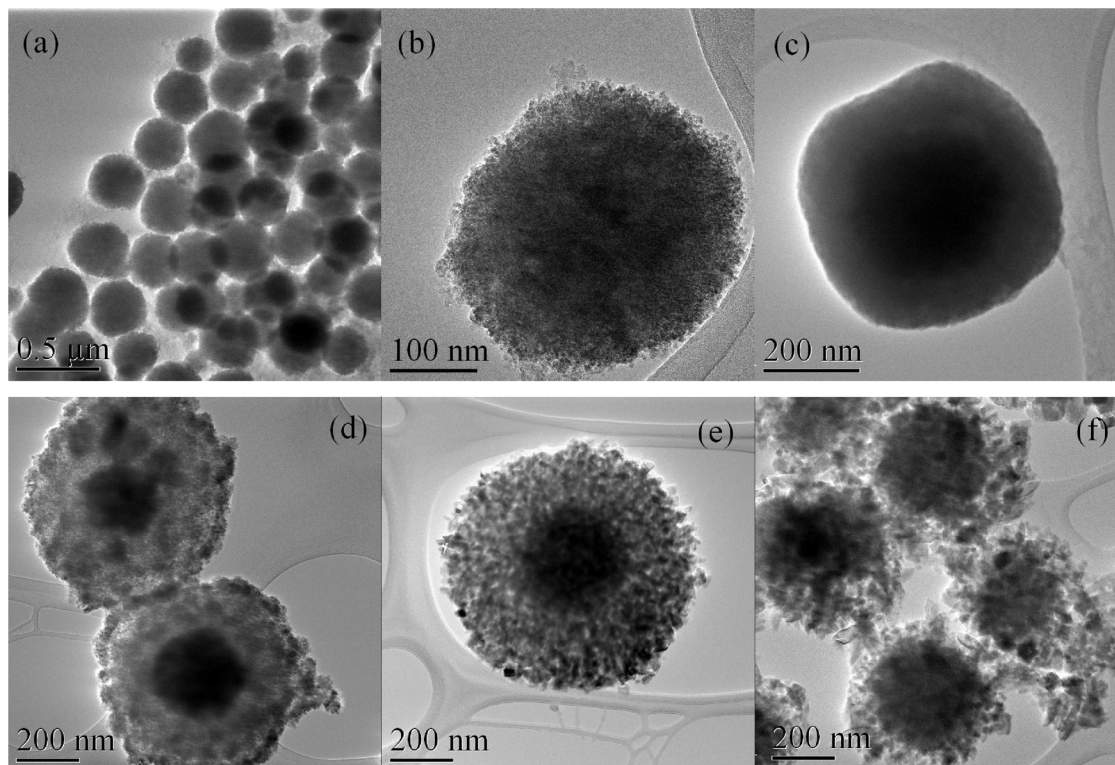


**Fig. 1.** (a) TEM and (b) magnified TEM images of  $\text{Fe}_3\text{O}_4$  microspheres. (c) TEM image of  $\text{Fe}_3\text{O}_4@TiO_2$  microspheres. TEM images of  $\text{Fe}_3\text{O}_4@mTiO_2$  microspheres prepared with different amounts of  $NH_3\cdot H_2O$ : (d) 1 mL, (e) 2 mL, and (f) 3 mL.



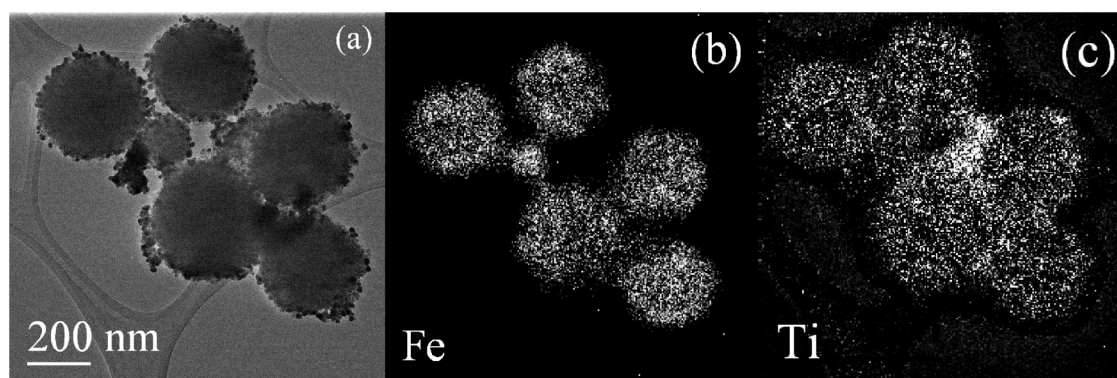


**Fig. 2.** (a) TEM image of  $\text{Fe}_3\text{O}_4@\text{mTiO}_2$  core-shell microspheres. (b) Fe and (c) Ti element mapping images of the same area (i.e. location) as in (a), using electron energy loss spectroscopy (EELS). They took the same image with different techniques, therefore they have the same magnification (i.e. have the same scale bar). b]

### 2.5. Antibacterial effect

The antibacterial effect of  $\text{Fe}_3\text{O}_4@\text{mTiO}_2$  and FTA3 core-shell microspheres under UV irradiation was investigated with bacteria *Escherichia coli* (DH5 $\alpha$ ), which are commonly used for the examination of antibacterial effect in water treatment. A frozen aliquot of the bacteria was inoculated into Brain heart infusion (BHI) broth, and cultured at 37 °C overnight under agitation. The bacteria were collected through centrifugation (3000 rpm, 10 min), and then re-suspended in sterile phosphate buffered saline (PBS). The concentration of the bacteria was adjusted to  $10^8$  cfu/mL.

10 mg  $\text{Fe}_3\text{O}_4@\text{mTiO}_2$  or FTA3 microspheres were added to a well (48-well plate) with 1 mL bacteria suspension. A well with only bacteria suspension was used as a control to show the bactericidal effect only under UV irradiation. UV irradiation (365 nm, 10 mW/cm<sup>2</sup>) was performed from the top of each well. The 48-well plate and the UV light were fixed onto an orbital shaking incubator, where 200 rpm shaking was performed to ensure well mixing of the microspheres in the bacteria suspension. A sample of 10  $\mu\text{L}$  suspension was taken from each well for bacterial viability analysis after UV irradiation for 10, 20, 30, 45 and 60 min. The tests were done in triplicate to ensure the reproduction.

The viability of photocatalytically treated bacteria samples was analyzed through resazurin test. Each sample was added to a well with 1 mL fresh BHI broth with resazurin (1.25  $\mu\text{g/mL}$ ). A standard curve with known bacterial concentration was made to quantify the viability of each treated sample. The plate was incubated at 37 °C for 3 h, and the transition from resazurin (blue, non-fluorescent) to resorufin (pink, fluorescent) due to the bacterial metabolism was detected with microplate fluorescent reader (Infinite 200,

Tecan, Switzerland) with the excitation and emission at 530 nm and 590 nm, respectively.

### 3. Results and discussion

The protocol for the fabrication of the  $\text{Fe}_3\text{O}_4@\text{mTiO}_2@\text{Au}$  microspheres is illustrated in Scheme 1. A compact  $\text{TiO}_2$  layer was directly deposited on the magnetite colloidal nanocrystal clusters ( $\text{Fe}_3\text{O}_4$ ) by a sol-gel method. The  $\text{Fe}_3\text{O}_4@\text{TiO}_2$  was then subjected to a hydrothermal treatment, which led to the formation of a mesoporous  $\text{TiO}_2$  ( $\text{mTiO}_2$ ) shell in crystal phase. The Au nanoparticles were deposited on the  $\text{Fe}_3\text{O}_4@\text{mTiO}_2$  microspheres through *in situ* reduction of perchloric acid. The size and density of Au nanoparticles were controlled by reaction temperature and precursor concentration, respectively.

The citrate-stabilized  $\text{Fe}_3\text{O}_4$  microspheres had spherical shape with a diameter of about 340 nm, as shown in Fig. 1 (a) and (b). The carboxyl groups in the citrate stabilizer provided the  $\text{Fe}_3\text{O}_4$  microspheres with outstanding dispersibility in polar solvents. During the next step of coating  $\text{TiO}_2$ , these groups adsorbed positive ammonium ions, which then drew the negatively charged  $\equiv\text{TiO}^-$  species, and thereby facilitated the direct deposition of titania via a sol-gel process [28,29]. (The existence of citrate will be further confirmed by thermogravimetric analysis.) As shown in Fig. 1 (c), a well-defined core-shell structure was obtained via a direct growth of  $\text{TiO}_2$  on  $\text{Fe}_3\text{O}_4$ . The crystallization and mesopore-creation of  $\text{TiO}_2$  shell took place simultaneously during the hydrothermal treatment of as-prepared  $\text{Fe}_3\text{O}_4@\text{TiO}_2$  in a mixed ethanol/water solvent, using  $\text{NH}_3\cdot\text{H}_2\text{O}$  as a porosity modifier. The dose of ammonia had a great effect on the porous structure of the  $\text{Fe}_3\text{O}_4@\text{mTiO}_2$  by adjusting

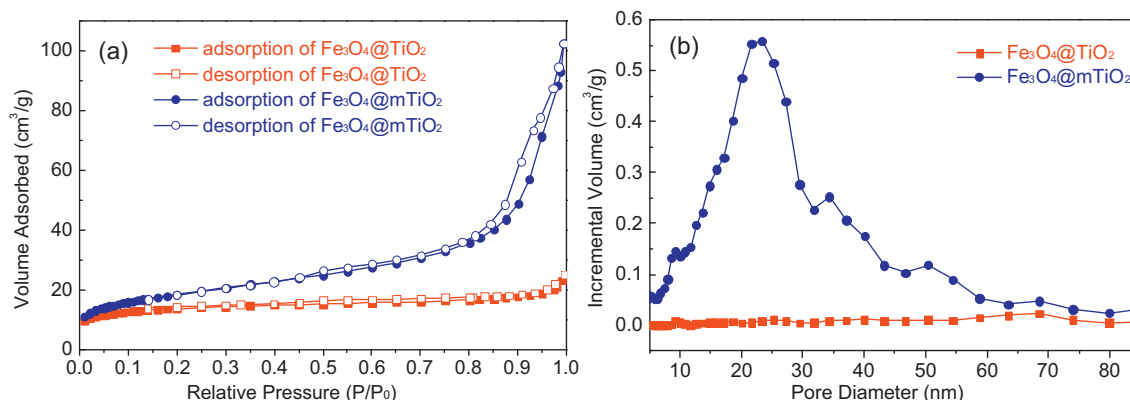


**Fig. 3.** (a)  $\text{N}_2$  adsorption-desorption isotherms and (b) BJH pore-size distribution curves for  $\text{Fe}_3\text{O}_4@\text{TiO}_2$  and  $\text{Fe}_3\text{O}_4@\text{mTiO}_2$  microspheres.

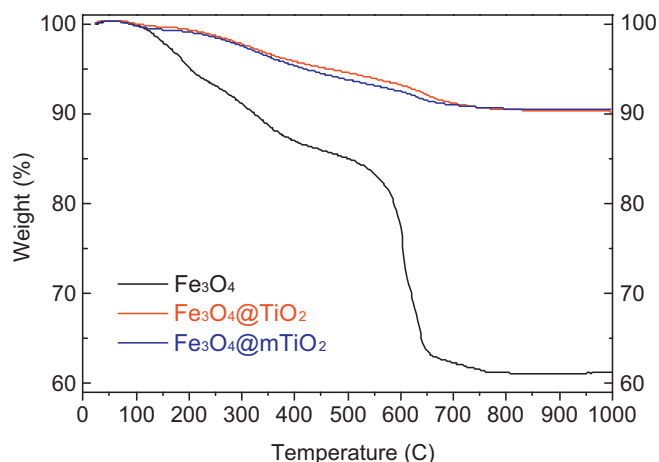


Fig. 4. TGA curves of  $\text{Fe}_3\text{O}_4$ ,  $\text{Fe}_3\text{O}_4@\text{TiO}_2$  and  $\text{Fe}_3\text{O}_4@m\text{TiO}_2$  microspheres.

the alkalinity of the solution and thereby tuning the crystal process [30]. When the ammonia was used to increase the alkalinity of the solution, the  $\text{OH}^-$  groups were enriched on the  $\text{TiO}_2$  surface. The adjacent  $\text{TiO}_2$  nanoparticles combined to form bigger ones through a dehydration reaction, leading to loose surface structure and large pore size [31]. Fig. 1 (d–f) shows the samples prepared with  $\text{NH}_3\cdot\text{H}_2\text{O}$  of 1 mL, 2 mL and 3 mL. The  $\text{TiO}_2$  shells appeared to have different textures. When the using amount of  $\text{NH}_3\cdot\text{H}_2\text{O}$  was increased, the porosity of the  $\text{TiO}_2$  shell was enhanced accordingly. The  $\text{TiO}_2$  shell prepared with 1 mL of  $\text{NH}_3\cdot\text{H}_2\text{O}$  was still dense, as shown in Fig. 1d. As 2 mL of  $\text{NH}_3\cdot\text{H}_2\text{O}$  was used, the round shape of the microsphere was kept well, and the porous structure of  $\text{TiO}_2$  shell clearly showed up (Fig. 1e). However, if the amount of  $\text{NH}_3\cdot\text{H}_2\text{O}$  was increased to 3 mL, the shape of  $\text{TiO}_2$  shell was partly damaged, numerous sheet-shaped  $\text{TiO}_2$  crystals were formed, and some of them became disjunctive from the peripheral surface (Fig. 1f). The excess  $\text{NH}_3\cdot\text{H}_2\text{O}$  did not benefit to the formation of intact porous shell. Therefore,  $\text{Fe}_3\text{O}_4@m\text{TiO}_2$  microspheres prepared using 2 mL of  $\text{NH}_3\cdot\text{H}_2\text{O}$  were chosen to further load Au nanoparticles.

In order to further confirm the distribution of both  $\text{Fe}_3\text{O}_4$  and  $\text{TiO}_2$ , the  $\text{Fe}_3\text{O}_4@m\text{TiO}_2$  microspheres were analyzed by electron mapping image analysis (Fig. 2) for the same microspheres with the same magnification. The images were acquired for Fe and Ti elements. For all the observed microspheres, Ti element shows a wider distribution over the Fe element, which indicates Fe locates at the inner part of these microspheres, but Ti lies in the outer layer (i.e. the well core–shell structure of  $\text{Fe}_3\text{O}_4@m\text{TiO}_2$  microspheres).

The  $\text{Fe}_3\text{O}_4@\text{TiO}_2$  and  $\text{Fe}_3\text{O}_4@m\text{TiO}_2$  microspheres were subjected to further study of their porous structure, by  $\text{N}_2$  adsorption–desorption analysis. As shown in Fig. 3a, the  $\text{Fe}_3\text{O}_4@\text{TiO}_2$  exhibited typical type II isotherm, which indicates that this sample was almost non-porous. However, the  $\text{Fe}_3\text{O}_4@m\text{TiO}_2$  showed typical type IV isotherm, indicative of its mesoporous character. Measured by BET model, the  $\text{Fe}_3\text{O}_4@\text{TiO}_2$  and  $\text{Fe}_3\text{O}_4@m\text{TiO}_2$  had surface areas of 49.2 and 66.1  $\text{m}^2/\text{g}$ , and pore volumes of 0.035 and 0.142  $\text{m}^3/\text{g}$ , respectively. The  $\text{Fe}_3\text{O}_4@m\text{TiO}_2$  had higher surface area and much larger volume than  $\text{Fe}_3\text{O}_4@\text{TiO}_2$ . Their corresponding pore-size distributions were evaluated using the Barrett–Joyner–Halenda (BJH) model, as shown in Fig. 3b. The  $\text{Fe}_3\text{O}_4@\text{TiO}_2$  did not show any pore distribution, while the pore distribution of the  $\text{Fe}_3\text{O}_4@m\text{TiO}_2$  centered at 23.4 nm. Judging from the small size of the  $\text{TiO}_2$  nanocrystals (as calculated from the XRD patterns, which will be discussed later), and TEM and  $\text{N}_2$  adsorption–desorption analyses, a possible hypothesis could be proposed: the mesoporosity might result from a number of

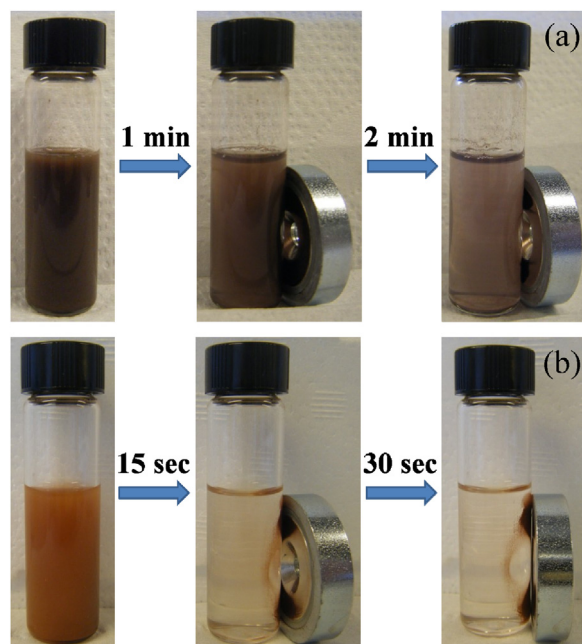


Fig. 5. Photos of (a)  $\text{Fe}_3\text{O}_4@\text{TiO}_2$  and (b)  $\text{Fe}_3\text{O}_4@m\text{TiO}_2$  microspheres in aqueous solutions with the same concentration (6 mg powder in 6 mL deionized water) before and after crystallization.

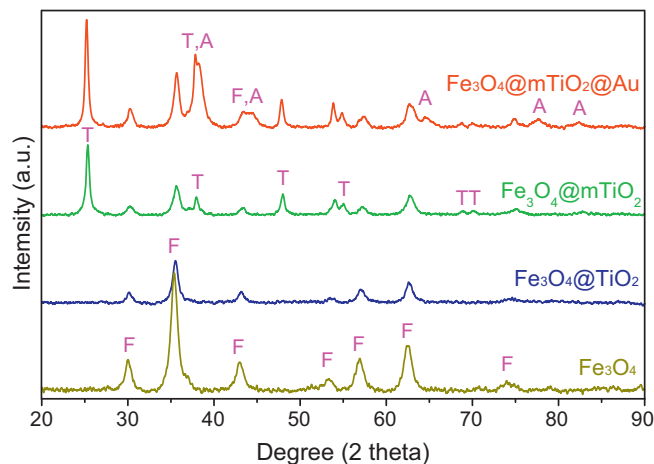
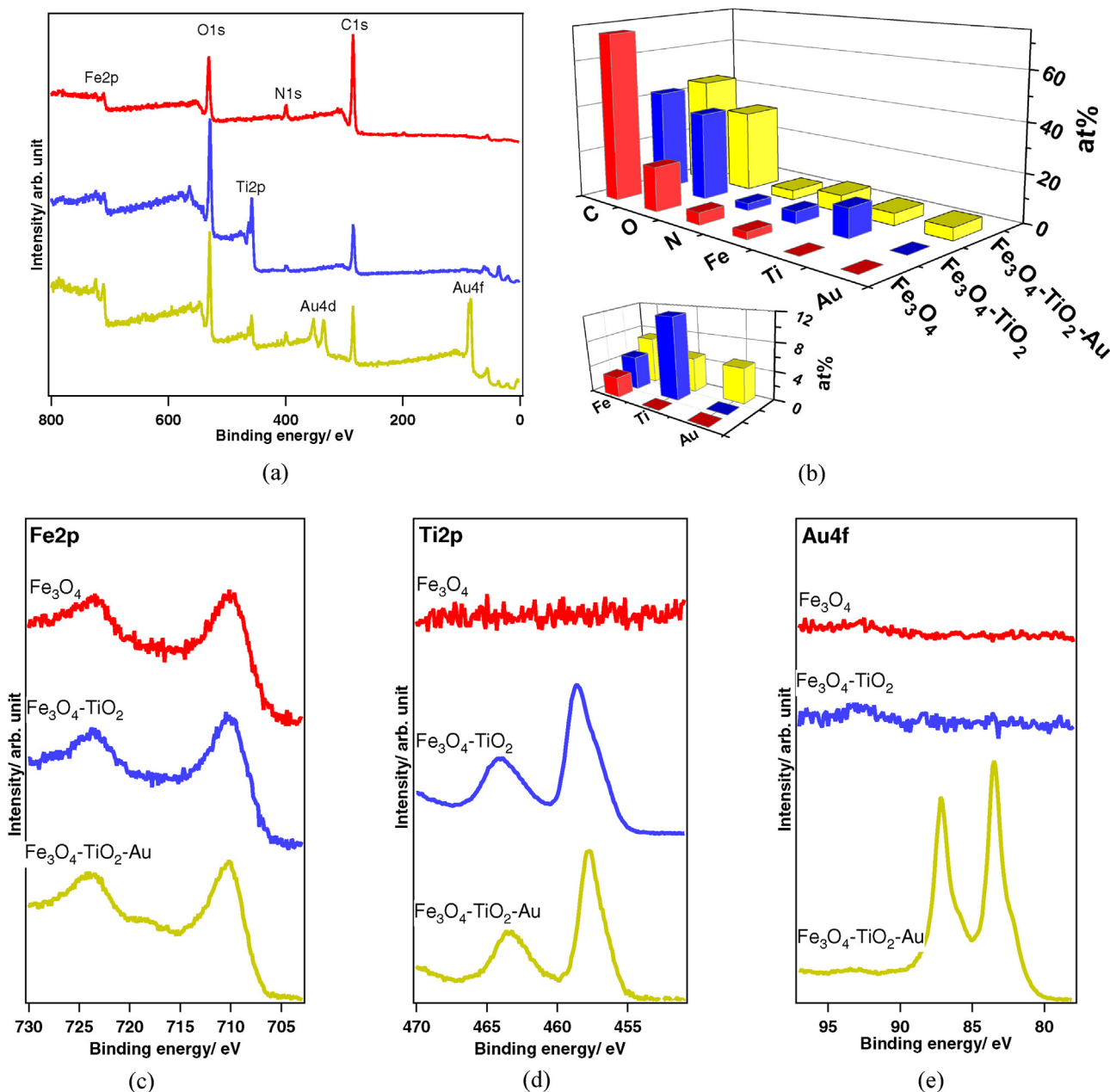


Fig. 6. XRD patterns of  $\text{Fe}_3\text{O}_4$ ,  $\text{Fe}_3\text{O}_4@\text{TiO}_2$ ,  $\text{Fe}_3\text{O}_4@m\text{TiO}_2$ , and  $\text{Fe}_3\text{O}_4@m\text{TiO}_2@\text{Au}$ . 3 mL (FTA3) microspheres. F, T, and A represent the diffraction peaks of  $\text{Fe}_3\text{O}_4$ ,  $\text{TiO}_2$ , and Au, respectively.

nanocrystals stacking with each other to form a shell, and simultaneously producing tiny slits between the neighboring primary nanocrystals in the shell.

The thermogravimetric analysis (TGA) of  $\text{Fe}_3\text{O}_4$  microspheres indicates that this sample contained 39.7 wt% of citrate stabilizer, which decomposed quickly around 600  $^\circ\text{C}$  (Fig. 4). These citrate molecules are present on the surface of the  $\text{Fe}_3\text{O}_4$ , facilitating the attachment of  $\text{TiO}_2$  in next step. According to the rough estimation based on the weight loss of citrate for  $\text{Fe}_3\text{O}_4@\text{TiO}_2$  and  $\text{Fe}_3\text{O}_4@m\text{TiO}_2$ , the  $\text{Fe}_3\text{O}_4$  contents in these two samples were 23.7% and 24.5%, so the  $\text{TiO}_2$  contents were 76.3% and 75.5%, respectively. Therefore, during the crystallization and pore-creation process,  $\text{NH}_3\cdot\text{H}_2\text{O}$  did not etch the  $\text{TiO}_2$  shell. In the real case, the  $\text{TiO}_2$  contents might be less than those values, since the citrate could have a loss during coating  $\text{TiO}_2$ .

Fig. 5 shows the magnetic response of  $\text{Fe}_3\text{O}_4@\text{TiO}_2$  and  $\text{Fe}_3\text{O}_4@m\text{TiO}_2$  microspheres in solution under an external



**Fig. 7.** (a) Survey scan of  $\text{Fe}_3\text{O}_4$ ,  $\text{Fe}_3\text{O}_4@\text{mTiO}_2$ , and FTA3 microspheres. (b) The surface compositions of all detectable elements (Fe, Ti, Au, C, O and N) in these samples. The compositions of Fe, Ti, and Au are zoomed in the bottom left corner. (c, d, e) Fine scans for Fe 2p, Ti 2p, and Au 4f of these samples.

magnetic field. The  $\text{Fe}_3\text{O}_4@\text{mTiO}_2$  microspheres with crystalline and mesoporous titania have stronger magnetic property than  $\text{Fe}_3\text{O}_4@\text{TiO}_2$ , and therefore are easier to be separated by a magnet. This might be ascribed to a strong shield effect of dense  $\text{TiO}_2$  layer in  $\text{Fe}_3\text{O}_4@\text{TiO}_2$ , while this effect from mesoporous  $\text{TiO}_2$  layer in  $\text{Fe}_3\text{O}_4@\text{mTiO}_2$  became weaker, due to its porous and open structure.

The crystal structures of  $\text{Fe}_3\text{O}_4$ ,  $\text{Fe}_3\text{O}_4@\text{TiO}_2$ ,  $\text{Fe}_3\text{O}_4@\text{mTiO}_2$ , and  $\text{Fe}_3\text{O}_4@\text{mTiO}_2@\text{Au}$  were studied by XRD (Fig. 6). All the diffraction peaks of  $\text{Fe}_3\text{O}_4$  microspheres can be readily indexed to the cubic phase of  $\text{Fe}_3\text{O}_4$  (JCPDS card No. 01-075-0449), marked as F in the figures. The average crystallite size of  $\text{Fe}_3\text{O}_4$  was 14.7 nm, which was calculated by using Scherrer's formula, based on five peaks at  $30.0^\circ$ ,  $35.3^\circ$ ,  $42.9^\circ$ ,  $57.0^\circ$  and  $62.4^\circ$ . Prior to the crystallization of the  $\text{TiO}_2$  shells, the  $\text{Fe}_3\text{O}_4@\text{TiO}_2$  microspheres showed almost the same XRD pattern as cubic structure of  $\text{Fe}_3\text{O}_4$ , and  $\text{TiO}_2$  coating only weakened the  $\text{Fe}_3\text{O}_4$  pattern. No characteristic  $\text{TiO}_2$  crystal peaks were

detected, indicative of an amorphous  $\text{TiO}_2$  shell formed around the  $\text{Fe}_3\text{O}_4$  core. After hydrothermal treatment, the  $\text{Fe}_3\text{O}_4@\text{mTiO}_2$  microspheres showed additional peaks, which can be assigned to anatase  $\text{TiO}_2$  (JCPDS card No. 01-075-2545), marked as T in the figures. Combining XRD with TEM and  $\text{N}_2$  adsorption-desorption results, the hydrothermal treatment fulfilled the crystal and porous formation of  $\text{TiO}_2$  shell. The average crystal size of  $\text{TiO}_2$  was about 28.9 nm, calculated from four peaks at  $25.3^\circ$ ,  $37.9^\circ$ ,  $48.0^\circ$  and  $53.9^\circ$ . Besides  $\text{Fe}_3\text{O}_4$  and  $\text{TiO}_2$  crystal patterns, the additional diffraction peaks in  $\text{Fe}_3\text{O}_4@\text{mTiO}_2@\text{Au}$  microspheres can be indexed to the cubic phase of Au (JCPDS card No. 00-004-0784), which are labeled as A in the figure. The average crystallite sizes of Au in the five samples (from FTA1 to FTA5) were calculated as 12.6 nm, 11.0 nm, 12.4 nm, 13.5 nm, and 12.6 nm, respectively, indicating the similar small size of Au primary crystallites in all the Au loaded samples.

The XPS survey scan (Fig. 7a) of the surface of  $\text{Fe}_3\text{O}_4$ ,  $\text{Fe}_3\text{O}_4@\text{mTiO}_2$ , and  $\text{Fe}_3\text{O}_4@\text{mTiO}_2@\text{Au}$  microspheres shows



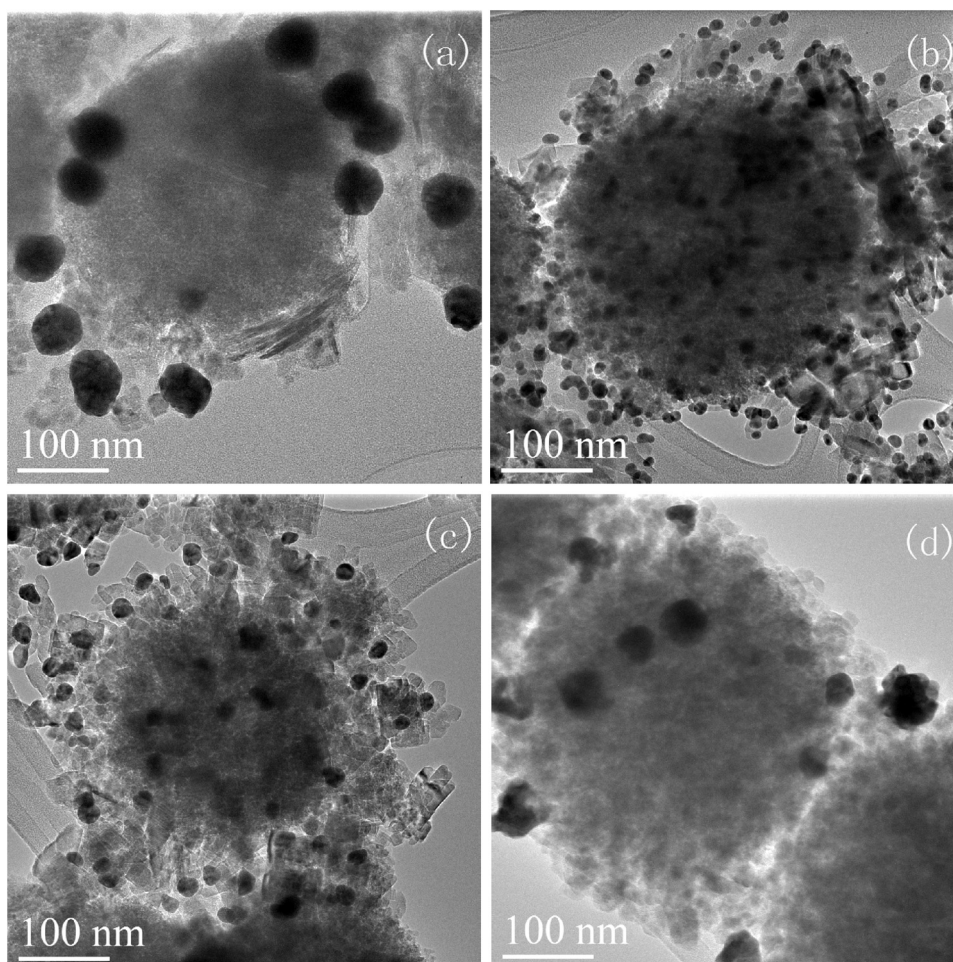


**Fig. 8.** TEM images of the  $\text{Fe}_3\text{O}_4@\text{mTiO}_2@\text{Au}$  microspheres prepared at different temperatures: (a) 60 °C, (b) 70 °C, (c) 80 °C, and (d) 90 °C.

the presence of elements, C, O, trace N (remained from the preparation step), Fe, Ti (only for  $\text{Fe}_3\text{O}_4@\text{mTiO}_2$  and  $\text{Fe}_3\text{O}_4@\text{mTiO}_2@\text{Au}$ ), and Au (only for  $\text{Fe}_3\text{O}_4@\text{mTiO}_2@\text{Au}$ ). All these samples contained Fe (Fig. 7c), confirmed by the binding energies of Fe  $2p_{3/2}$  and  $2p_{1/2}$  at  $\sim 710$  eV and  $\sim 724$  eV, respectively. These binding energies can be assigned to  $\text{Fe}_3\text{O}_4$  [32]. Interestingly, the surface concentration of Fe increased from  $\text{Fe}_3\text{O}_4$  to  $\text{Fe}_3\text{O}_4@\text{mTiO}_2$ , and then further to  $\text{Fe}_3\text{O}_4@\text{mTiO}_2@\text{Au}$  (Fig. 7b). This might be ascribed to the partial removal of citrate stabilizer during the coating of  $\text{TiO}_2$  and Au, which can also be confirmed by the large decrease in the surface C content after coating of  $\text{TiO}_2$  and Au (see Figs. 7a and 7b). After coating  $\text{Fe}_3\text{O}_4$  by  $\text{TiO}_2$ ,  $\text{Fe}_3\text{O}_4@\text{mTiO}_2$  showed the signals of Ti  $2p_{3/2}$  and Ti  $2p_{1/2}$  at  $\sim 458$  eV and  $\sim 464$  eV, respectively (Fig. 7d), corresponding to  $\text{TiO}_2$  [33]. The surface concentration of O increased, due to  $\text{TiO}_2$  coating. Metallic Au loading can be confirmed by the presence of the signals of Au  $4f_{7/2}$  and Au  $4f_{5/2}$  at  $\sim 83.5$  eV and  $\sim 87$  eV in  $\text{Fe}_3\text{O}_4@\text{mTiO}_2@\text{Au}$ , respectively (Fig. 7e) [33]. Au loading decreased the surface contents of Ti and O in  $\text{Fe}_3\text{O}_4@\text{mTiO}_2@\text{Au}$ , compared to those in  $\text{Fe}_3\text{O}_4@\text{mTiO}_2$ .

Since temperature normally has a large effect on the reduction of Au precursors, the preparation of  $\text{Fe}_3\text{O}_4@\text{mTiO}_2@\text{Au}$  microspheres at varied temperatures was studied, as shown in Fig. 8. At the reaction temperature of 60 °C, the size of Au nanoparticles was in the range of 40–60 nm. While at 70 °C and 80 °C, Au nanoparticles were much smaller and more uniform, and had narrow distribution with the size in the range of 10–15 nm and 15–20 nm, respectively. However, the Au nanoparticles prepared at 90 °C had larger size in the range of 20–50 nm. It is well known that the

size of the Au nanocrystals depends on the relative rate of the crystal nucleation and growth. When the temperature was too low, the rate of crystal nucleation was slow. Few crystal nucleuses were created and big crystals were obtained after the crystal growth on those limited nucleuses. While the temperature was too high, fast crystal growth and serious aggregation also led to big crystals. Since small Au nanoparticles can effectively modify  $\text{TiO}_2$  properties, 70 °C was chosen to prepare  $\text{Fe}_3\text{O}_4@\text{mTiO}_2@\text{Au}$  microspheres with different Au loading amounts. Energy dispersive X-ray (EDX) spectroscopy also confirmed Au loading and the right composition of  $\text{Fe}_3\text{O}_4@\text{mTiO}_2@\text{Au}$  microspheres (Fig. S1 in SI).

Fig. 9 presents the TEM images of  $\text{Fe}_3\text{O}_4@\text{mTiO}_2@\text{Au}$  microspheres synthesized with different amounts of  $\text{HAuCl}_4$  solution. When the used  $\text{HAuCl}_4$  solution was 1 mL in the synthesis, a few Au nanoparticles were loaded with good distribution in the  $\text{TiO}_2$  shell, as shown in Fig. 9a. While  $\text{HAuCl}_4$  solutions of 2 mL and 3 mL were used, the density of Au nanoparticles increased, as shown in Fig. 9(b) and (c), respectively. However, when the used  $\text{HAuCl}_4$  solution increased to 4 mL and 5 mL, the density of Au nanoparticles did not increase obviously, and some aggregates were observable, as shown in Fig. 9(d) and (e), respectively. As there was too high concentration of  $\text{Au}^{3+}$  ions in the solution, after adding excess  $\text{NaBH}_4$ , the ions were fast reduced, resulting in a certain aggregation, and some big Au particles might drop off from the  $\text{mTiO}_2$  shell. Fig. 9(f) presents a magnified TEM image of Au nanoparticles embedded in the  $\text{mTiO}_2$  shell. The Au nanoparticles had an average diameter of 15 nm with a good dispersion in the  $\text{TiO}_2$  shell.

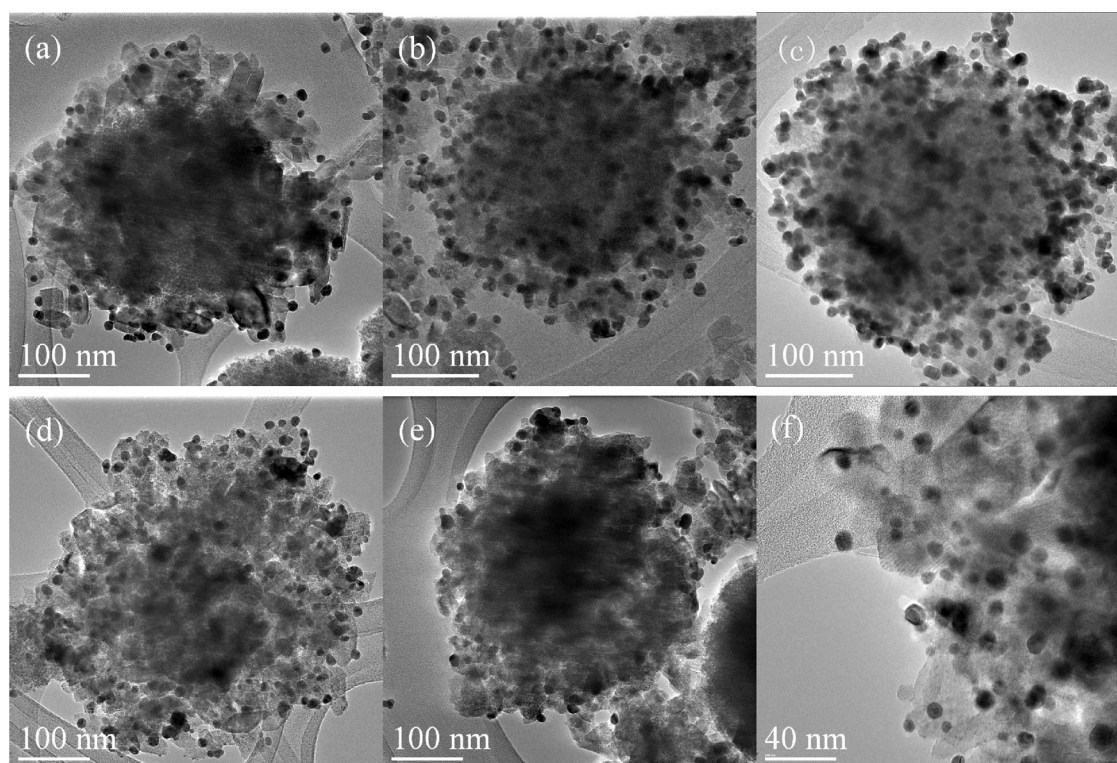


**Fig. 9.** TEM images of  $\text{Fe}_3\text{O}_4@\text{mTiO}_2@\text{Au}$  microspheres synthesized using different volumes of  $\text{HAuCl}_4$  solution: (a) 1 mL, (b) 2 mL, (c) 3 mL, (d) 4 mL, and (e) 5 mL. (f) Magnified image of (b), showing the Au nanoparticles embedded in the  $\text{mTiO}_2$  shell.

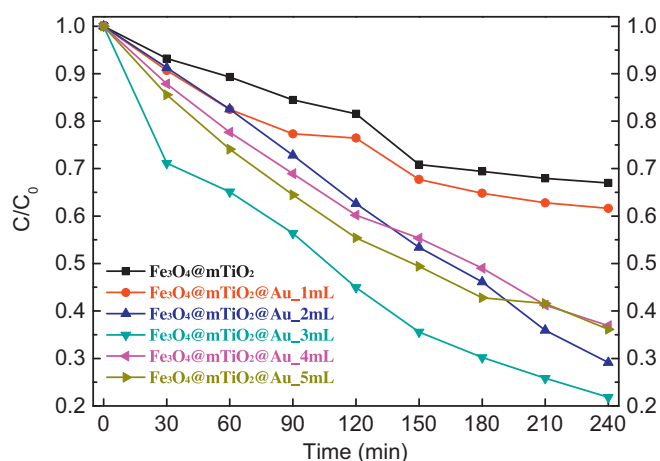


**Fig. 10.** The photocatalytic degradation of MB by  $\text{Fe}_3\text{O}_4@\text{mTiO}_2@\text{Au}$  microspheres with different Au loading amounts.

Fig. 10 shows the photocatalytic activity of the prepared core-shell microspheres and the influence of different Au loading on it. It is clearly observed that the crystal  $\text{TiO}_2$  shell of the microspheres had photocatalytic effect, and the decoration of  $\text{TiO}_2$ -based photocatalysts with Au nanoparticles was an effective way to achieve higher catalytic efficiency, since all the Au loaded samples showed higher photocatalytic activity than  $\text{Fe}_3\text{O}_4@\text{mTiO}_2$ . After 4 h photocatalytic degradation under the UV radiation, the remaining MB ( $C/C_0 = I/I_0$ ) for  $\text{Fe}_3\text{O}_4@\text{mTiO}_2$ , FTA1, FTA2, FTA3, FTA4, and FTA5 was 0.67, 0.62, 0.29, 0.22, 0.37, and 0.36, respectively. FTA3 showed the best photocatalytic efficiency, about 2.38 times higher than  $\text{Fe}_3\text{O}_4@\text{mTiO}_2$  microspheres. The low density and/or large

size (only for FTA5) of Au nanoparticles on  $\text{TiO}_2$  surfaces may limit the promoting effect of Au decoration in samples FTA1, FTA2 and FTA5, while the surface modification by uniform and dense Au nanoparticles can enhance photocatalytic efficiency to a large degree in samples FTA2 and FTA3. It should be pointed out that all the core-shell microspheres can be quickly re-collected with the help of a magnetic field. To explore our samples for practical applications, the catalytic stability of our samples was tested. After magnetic separation and simple treatment,  $\text{Fe}_3\text{O}_4@\text{mTiO}_2$  (unmodified) and FTA3 (Au modified) exhibited stable catalytic performance after running six cycles, as shown in Table 1.

Photocatalysis has been proved an effective antibacterial strategy, and this has been applied in water treatment and air purification, and on antibacterial surfaces of biomedical devices. The photocatalytic bactericidal effect originates from the lipid peroxidation due to the interaction between the unsaturated lipid in bacterial cell membrane and the reactive oxygen species (ROS) produced in photocatalysis [34,35]. Fig. 11 shows the antibacterial effect of  $\text{Fe}_3\text{O}_4@\text{mTiO}_2$  and FTA3 microspheres under UV irradiation. Although UV irradiation itself was lethal to bacteria, however, the photocatalysis driven by  $\text{Fe}_3\text{O}_4@\text{mTiO}_2$  and FTA3 microspheres led to much faster bacterial inactivation. FTA3 microspheres showed higher photocatalytically bactericidal efficiency

**Table 1**  
Photocatalytic activity for reuses of the photocatalysts.

| Reuse                                 | 1                 | 2    | 3    | 4    | 5    | 6    |
|---------------------------------------|-------------------|------|------|------|------|------|
| $\text{Fe}_3\text{O}_4@\text{mTiO}_2$ | 33.0 <sup>a</sup> | 32.1 | 31.9 | 31.3 | 32.7 | 32.2 |
| FTA3                                  | 78.2              | 77.1 | 77.9 | 77.8 | 77.4 | 76.9 |

<sup>a</sup> All the values in the table show the degradation percentage of MB by reusing the photocatalysts under the same condition as in Fig. 10.



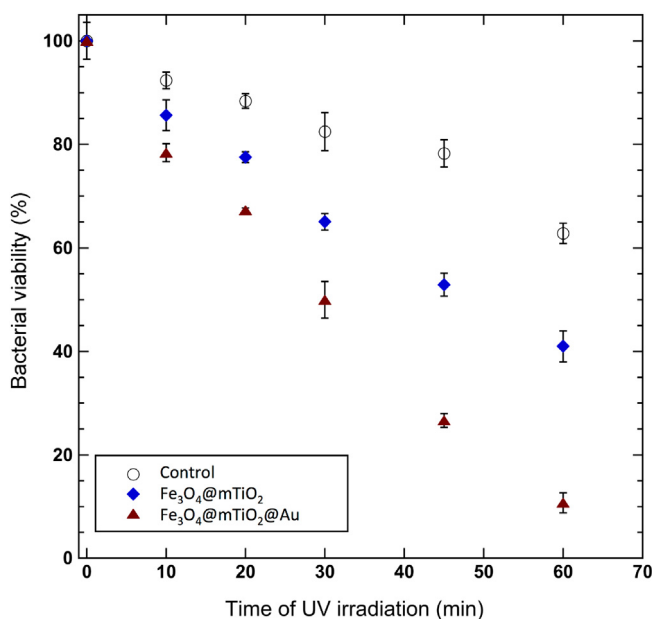


**Fig. 11.** Antibacterial effect of Fe<sub>3</sub>O<sub>4</sub>@mTiO<sub>2</sub> and FTA3 microspheres under UV irradiation.

than Fe<sub>3</sub>O<sub>4</sub>@mTiO<sub>2</sub>, due to the surface decoration by Au nanoparticles, as in the case of MB photocatalytic degradation. After 1 h, the viability of bacteria *E. coli* was reduced by 59.9% and 89.3% in the test with Fe<sub>3</sub>O<sub>4</sub>@mTiO<sub>2</sub> and FTA3, respectively.

#### 4. Conclusion

Herein, a hierarchical structure of Fe<sub>3</sub>O<sub>4</sub>@mTiO<sub>2</sub>@Au with Fe<sub>3</sub>O<sub>4</sub> magnetic microsphere as a core, mesoporous crystalline TiO<sub>2</sub> as a shell, and Au nanoparticles embedded in the shell is presented. The structure and performance of these microspheres can be finely tuned during the preparation. NH<sub>3</sub>·H<sub>2</sub>O using amount can largely affect the mesoporous structure of TiO<sub>2</sub>, and the reduction temperature of Au precursor determined the size and dispersion of Au nanoparticles on the TiO<sub>2</sub> surface. Fe<sub>3</sub>O<sub>4</sub>@mTiO<sub>2</sub>@Au showed higher photocatalytic activity in MB degradation and bactericidal test, in comparison with the Au-uncoated sample, Fe<sub>3</sub>O<sub>4</sub>@mTiO<sub>2</sub> microspheres. These Fe<sub>3</sub>O<sub>4</sub>@mTiO<sub>2</sub>@Au microspheres can be expected as recyclable photocatalysts for environmental treatment.

#### Acknowledgments

This work was financially supported by Ångpanneföreningen's Foundation for Research and Development, the Swedish Association of Graduate Engineers, and Opening Project from the Key Laboratory for Ultrafine Materials of the Ministry of Education in East China University of Science and Technology.

#### Appendix A. Supplementary data

Supplementary data associated with this article can be found, in the online version, at <http://dx.doi.org/10.1016/j.apcatb.2014.03.031>.

#### References

- [1] M.R. Hoffmann, S.T. Martin, W. Choi, D.W. Bahnemann, *Chem. Rev.* 95 (1995) 69–96.
- [2] A.L. Linsebigler, G. Lu, J.T. Yates, *Chem. Rev.* 95 (1995) 735–758.
- [3] D. Chen, L. Cao, F. Huang, P. Imperia, Y.-B. Cheng, R.A. Caruso, *J. Am. Chem. Soc.* 132 (2010) 4438–4444.
- [4] J. Zhu, J. Zhang, F. Chen, K. Iino, M. Anpo, *Top. Catal.* 35 (2005) 261–268.
- [5] J. Zhu, J. Zhang, F. Chen, M. Anpo, *Mater. Lett.* 59 (2005) 3378–3381.
- [6] H.Y. Yang, S.F. Yu, S.P. Lau, X. Zhang, D.D. Sun, G. Jun, *Small* 5 (2009) 2260–2264.
- [7] H. Zhu, B. Yang, J. Xu, Z. Fu, M. Wen, T. Guo, S. Fu, J. Zuo, S. Zhang, *Appl. Catal. B: Environ.* 90 (2009) 463–469.
- [8] L. Yang, S. Luo, Y. Li, Y. Xiao, Q. Kang, Q. Cai, *Environ. Sci. Technol.* 44 (2010) 7641–7646.
- [9] P. Sangpour, F. Hashemi, A.Z. Moshfegh, *J. Phys. Chem. C* 114 (2010) 13955–13961.
- [10] P. Fu, P. Zhang, *Appl. Catal. B: Environ.* 96 (2010) 176–184.
- [11] R. Sellappan, J. Zhu, H. Fredriksson, R.S. Martins, M. Zäch, D. Chakarov, *J. Mol. Catal. A: Chem.* 335 (2011) 136–144.
- [12] P.M. Álvarez, J. Jaramillo, F. López-Piñero, P.K. Plucinski, *Appl. Catal. B: Environ.* 100 (2010) 338–345.
- [13] S. Xuan, W. Jiang, X. Gong, Y. Hu, Z. Chen, *J. Phys. Chem. C* 113 (2008) 553–558.
- [14] J.F. Zhu, M. Zach, *Curr. Opin. Colloid Interface Sci.* 14 (2009) 260–269.
- [15] J. Sá, M. Fernández-García, J.A. Anderson, *Catal. Commun.* 9 (2008) 1991–1995.
- [16] R. Su, P. Tiruvalam, Q. He, N. Dimitratos, L. Kesavan, C. Hammond, J.A. Lopez-Sanchez, R. Bechstein, C.J. Kiely, G.J. Hutchings, F. Besenbacher, *ACS Nano* 6 (2012) 6284–6292.
- [17] F.L. Zhang, Y.H. Zheng, Y.N. Cao, C.Q. Chen, Y.Y. Zhan, X.Y. Lin, Q. Zheng, K.M. Wei, J.F. Zhu, *J. Mater. Chem.* 19 (2009) 2771–2777.
- [18] C. Gomes Silva, R. Juárez, T. Marino, R. Molinari, H. García, *J. Am. Chem. Soc.* 133 (2010) 595–602.
- [19] J. Zhu, D. Chakarov, M. Zäch, in: L. Zang (Ed.), *Energy Efficiency and Renewable Energy Through Nanotechnology*, Springer, London, 2011, pp. 441–486.
- [20] M. Hosseini, M.M. Momeni, M. Faraji, *J. Mol. Catal. A: Chem.* 335 (2011) 199–204.
- [21] X.Z. Li, F.B. Li, *Environ. Sci. Technol.* 35 (2001) 2381–2387.
- [22] J. Shen, Y. Zhu, X. Yang, C. Li, *J. Mater. Chem.* 22 (2012) 13341–13347.
- [23] W. Hu, B. Liu, Q. Wang, Y. Liu, Y. Liu, P. Jing, S. Yu, L. Liu, J. Zhang, *Chem. Commun.* 49 (2013) 7596–7598.
- [24] S. Gaur, S. Johansson, F. Mohammad, C.S.S.R. Kumar, J.J. Spivey, *J. Phys. Chem. C* 116 (2012) 22319–22326.
- [25] J. Liu, Z. Sun, Y. Deng, Y. Zou, C. Li, X. Guo, L. Xiong, Y. Gao, F. Li, D. Zhao, *Angew. Chem. Int. Ed.* 48 (2009) 5875–5879.
- [26] W. Ma, S. Xu, J. Li, J. Guo, Y. Lin, C. Wang, *J. Polym. Sci. Part A: Polym. Chem.* 49 (2011) 2725–2733.
- [27] W.-F. Ma, Y. Zhang, L.-L. Li, L.-J. You, P. Zhang, Y.-T. Zhang, J.-M. Li, M. Yu, J. Guo, H.-J. Lu, C.-C. Wang, *ACS Nano* 6 (2012) 3179–3188.
- [28] P. Wang, D. Chen, F.-Q. Tang, *Langmuir* 22 (2006) 4832–4835.
- [29] Z.-Y. Shen, L.-Y. Li, Y. Li, C.-C. Wang, *J. Colloid Interface Sci.* 354 (2011) 196–201.
- [30] J. Yu, Y. Su, B. Cheng, M. Zhou, *J. Mol. Catal. A: Chem.* 258 (2006) 104–112.
- [31] B. Liu, K. Nakata, M. Sakai, H. Saito, T. Ochiai, T. Murakami, K. Takagi, A. Fujishima, *Catal. Sci. Technol.* 2 (2012) 1933–1939.
- [32] T. Yamashita, P. Hayes, *Appl. Surf. Sci.* 254 (2008) 2441–2449.
- [33] D. Zhang, G. Li, F. Wang, J.C. Yu, *CrystEngComm* 12 (2010) 1759–1763.
- [34] O.K. Dalrymple, E. Stefanakos, M.A. Trotz, D.Y. Goswami, *Appl. Catal. B: Environ.* 98 (2010) 27–38.
- [35] H. Foster, I. Ditta, S. Varghese, A. Steele, *Appl. Microbiol. Biotechnol.* 90 (2011) 1847–1868.